Tuning Core-Shell Interactions in Tungsten Carbide–Pt Nanoparticles for the Hydrogen Evolution Reaction

Journal:	*Physical Chemistry Chemical Physics*
Manuscript ID	CP-ART-06-2018-004113.R1
Article Type:	Paper
Date Submitted by the Author:	28-Aug-2018
Complete List of Authors:	Jain, Akash; University of Massachusetts, USA Ramasubramaniam, Ashwin; University of Massachusetts, USA,

Tuning Core-Shell Interactions in Tungsten Carbide-Pt Nanoparticles for the Hydrogen Evolution Reaction

Akash Jain[1] and Ashwin Ramasubramaniam[2,*]

[1] Department of Chemical Engineering, University of Massachusetts, Amherst, MA 01003, U.S.A.

[2] Department of Mechanical and Industrial Engineering, University of Massachusetts, Amherst, MA 01003, U.S.A.

ABSTRACT

Platinum (Pt) is among the best electrocatalysts for the hydrogen evolution reaction (HER), a potentially fossil-free route for hydrogen production. Reduction in Pt loading and overall catalyst cost, without sacrificing catalytic activity, can be achieved by the synthesis of stable core-shell nanoparticles of transition-metal carbides and Pt. We employ density-functional theory (DFT) calculations to study and contrast the suitability of the α and β phases of tungsten carbide (WC) as support (core) materials for Pt shells. We examine the thermodynamic stability of 1-2 layers of Pt on α- and β-WC surfaces, carefully accounting for the delicate balance between epitaxial mismatch strains and chemical bonding between cores and shells. We also study the effects of alloying β-WC with Ti to modulate the stability and electronic structure of the core-shell structures. We compare the electronic structures of Pt overlayers supported on α-WC and β-$Ti_xW_{1-x}C$ surfaces and compare their activities for HER using the hydrogen binding energy as a descriptor of catalytic activity. Our studies reveal that moderate Ti doping of the metastable β-WC phase significantly improves its stability and, with merely two layers of Pt loading, HER activity comparable or superior to Pt (111) can be attained. Overall, our results provide detailed

insight into experimental observations of the excellent stability and high catalytic activity of β-$Ti_xW_{1-x}C$@Pt core-shell nanoparticles.

Keywords: transition-metal carbides, heterogeneous catalysis, hydrogen evolution reaction, density functional theory

Corresponding Author

* ashwin@engin.umass.edu

1. INTRODUCTION

Transition-metal carbides (TMCs) are promising catalysts for several chemical reactions such as hydrogenation, oxygenation, isomerization, Fischer-Tropsch reaction, water-gas shift, hydrogen evolution (HER), and CO_2 reduction (CRR), among others.[1–9] These materials display properties common to ceramics and metals including high melting points, extreme hardness, and high thermal and electronic conductivity. Early interest in TMC as catalysts emerged from observations of the so-called "platinum-like" catalytic behavior of tungsten carbides,[8] which then spawned further work on TMCs as inexpensive, earth-abundant replacements for noble metal catalysts. Recent studies show that TMCs, which display mixed *p* and *d* valence-electron character, might offer a promising route toward breaking the tight constraints of scaling relationships on transition-metal alloy surfaces.[10–12]

Apart from being promising catalysts in their own right, TMCs serve as excellent supports for other transition-metal catalysts, either as cores for core-shell nanoparticles[13–15] or as bulk-like supports.[1,5,16] In particular, there has been much recent interest in employing transition-metal carbides as supports for Pt,[17] which is among the best known catalysts for the hydrogen evolution reaction (HER) via water splitting.[18, 19] When integrated with renewable sources of energy, HER can offer a fossil-fuel free route for hydrogen production. Yet, the cost and scarcity of Pt (or similar noble metals) as well as operational problems such as catalyst sintering, corrosion of the support, and weak affinity between Pt and its support material [20, 21] motivate the search for improved catalysts for HER. Several density functional theory (DFT) studies have reported that a single monolayer (ML) of Pt deposited over a WC support has HER activity similar to the Pt (111) surface.[16,22–24] Additionally, Pt is reported to be more stable on the metal (W) terminated WC (0001) surface than on graphene supports.[16,25–27] In an effort to minimize the use of precious

Pt catalyst while maximizing the effective surface area, Hsu *et al*. synthesized few-layer Pt shells on WC cores [28,29] as well as few-layer Pt on planar WC surfaces.[30,31] More recently, Hunt *et al*. devised a method to synthesize highly stable and catalytically active TiWC@Pt and TiWN@Pt core-shell nanoparticles with precise control over the size and composition of the nanoparticle core as well as the thickness of the shell (down to 1 ML).[15,32–34] These synthetic advances minimize the use of expensive Pt while maximizing the effective surface area of the catalyst.

From the theoretical perspective, HER has been studied for Pt monolayers (ML) on hexagonal-close-packed WC (α-WC; room-temperature phase) supports;[16,18,22–24,35,36] such models provide a reasonable approximation of core-shell α-WC@Pt nanoparticles and planar Pt/α-WC synthesized by Hsu *et al*.[28–31] On the other hand, the core-shell nanoparticles synthesized by Hunt *et al*.,[15,32–34] display the face-centered-cubic phase of WC (β-WC; stable above 2525°C [37]). As the electronic properties of α-WC and β-WC are fundamentally different,[14,38,39] the electronic and catalytic properties of supported Pt MLs could also vary substantially as a function of the underlying support. Indeed, Yates *et al*.[14] performed DFT studies of oxygen adsorption on Pt overlayers on α-WC and β-WC and found that a Pt ML over β-WC binds O atoms more strongly than the Pt (111) surface, rendering the former a poorer catalyst for oxygen reduction (ORR); on the other hand, a Pt ML over α-WC was predicted to bind O as strongly as Pt (111) making it more suited for ORR. Hendon *et al.*[13] reported electronic structures of several β-$Ti_{0.1}W_{0.9}C$–supported noble-metal overlayers with different surface coverages and showed that the *d*-band centers of the surfaces vary as a function of the surface topology and thickness of the overlayers. To date, we are unaware of any systematic studies of Pt MLs over α-WC and β-WC in relation to the HER, which is the focus of this paper.

In this work, we employ DFT calculations to compare the thermodynamic stability, electronic structure and HER catalytic activity of various Pt/WC surfaces and thereby contrast the suitability of α- and β-WC as support (core) materials for WC@Pt core-shell nanoparticles for HER. We also examine the role of Ti in stabilizing and modulating the catalytic properties of β-WC@Pt core-shell nanoparticles in light of recent experiments along these lines.[15,33,34] We find that the formation of β-WC@Pt core-shell nanoparticles is thermodynamically preferred over α-WC@Pt, and that doping β-WC with Ti further improves the stability of Pt/WC interface without affecting the desirable electronic properties of the Pt MLs. Comparisons of HBEs, a commonly employed descriptor of HER catalytic activity, on 1-2 MLs of Pt supported on α- and (Ti-doped) β-WC reveal a substantial support effect, which we explain via a detailed electronic structure analysis. Based on our studies, 2 MLs of Pt supported on β-$Ti_{0.125}W_{0.875}C$ (111) are predicted to attain HER activities comparable to Pt (111), making β-WC@Pt a promising system for further exploration as a highly active yet inexpensive HER catalyst.

2. COMPUTATIONAL METHODS

DFT calculations were performed using the Vienna *Ab-Initio* Simulation Package (VASP; version 5.4.1). [40,41] The projector-augmented wave (PAW) method [42,43] was used to describe the core and valence electrons in conjunction with the Perdew-Burke-Ernzerhof [44] form of the generalized-gradient approximation for electron exchange and correlation. The valence electron configurations employed for Pt, W, Ti, and C are $6s^1 5d^9$, $6s^2 5d^4$, $4s^2 3d^2$, and $2s^2 2p^2$, respectively. Total energies were converged to within 1 meV/atom by choosing a planewave kinetic-energy cutoff of 500 eV and sampling the Brillouin zone with sufficiently dense Γ-centered *k*-point meshes. Specifically, we used 21×21×21 *k*-point meshes for the reference bulk phases of Pt (fcc),

Ti (hcp), W (bcc), α-WC, and β-WC, and 21×21×1 *k*-points for C (graphene). For the slab models, we used 11×11×1 *k*-points for Pt (111); 7×7×1 *k*-points for α -WC (001), $Pt_{1,\ 2\ MLs}$/α -WC (001), β-WC (001) and β-$Ti_xW_{1-x}C$ (111); 8×4×1 *k*-points for Pt_{ML}/β-WC (001); and 5×3×1 *k*-points for $Pt_{1,\ 2\ MLs}$/β-$Ti_xW_{1-x}C$ (111). Brillouin-zone integrations were performed with a Methfessel-Paxton smearing [45] of 0.1 eV. Structural optimization was performed with a tolerance of 0.01 eV/Å for the Hellman-Feynman force on each atom. Structural optimization of the bulk phases was performed by relaxing lattice vectors as well as ionic positions; the optimized lattice parameters were used to build slab models for further studies.

In our slab calculations, the Pt (111) slab consisted of five layers while the α-WC and β-WC slabs consisted of seven and eleven layers, respectively; periodic images of the slabs were separated by at least 10 Å of vacuum in the normal direction to avoid spurious image interactions. Pt/WC slabs were created by placing 1 or 2 MLs of Pt atoms on the WC slabs. Formation and interface energies of $Pt_{1,\ 2\ MLs}$/α-WC and $Pt_{1,\ 2\ MLs}$/β-$Ti_xW_{1-x}C$ interfaces, were calculated using symmetric slabs (with Pt on both surfaces) to avoid net dipoles within the supercell; during structural optimization, the three middle layers of the slabs were held frozen to simulate the bulk constraint. Details of the various Pt/WC supercells are provided in Table S1.

For calculations of hydrogen-binding energies (HBE), 3×3×1 supercells were used for all slabs except for Pt_{ML}/β-WC (001) and $Pt_{1,\ 2\ MLs}$/β-$Ti_xW_{1-x}C$ (111) for which we used the (large) unit cells listed in Table S1. To reduce the computational cost, we used asymmetric slabs for these calculations and held the three bottommost layers fixed to simulate the bulk constraint; dipole corrections [46,47] were applied normal to the slabs. HBEs were calculated by adsorbing a single H atom at various inequivalent surface sites; HBEs at the most stable sites are reported in this paper. The HBE of the catalyst is defined as

$$HBE = E_{Slab+H} - E_{slab} - E_{H_2}/2 + \Delta E_{ZPE}, \quad (1)$$

where E_{Slab+H}, E_{Slab} and E_{H_2} are the total energies of the slab with an adsorbed H atom, the slab itself, and the (gas-phase) H_2 molecule. ΔE_{ZPE} is the zero-point energy correction for the adsorbed H atom, calculated as the difference between the zero-point energy of an adsorbed H atom and its corresponding value in the H_2 molecule. The zero-point energy in each case is obtained by perturbing the H atom from its equilibrium position by ±0.015 Å in all three Cartesian directions, diagonalizing the mass-weighted Hessian matrix to calculate the vibrational frequencies ω_i, and evaluating the sum $E_{ZPE} = \sum_i \hbar\omega_i / 2$.

Finally, to obtain insights into the electronic structure of the supported Pt monolayers—in particular, their *d*-band centers—atom-projected partial densities of states were calculated with VASP using 1500 energy grid points. The average *d*-band center, E_d, relative to the Fermi level, E_F, was calculated as,[48]

$$E_d - E_F = \frac{\int_{-\infty}^{E_F} E\, n_d(E)\, dE}{\int_{-\infty}^{E_F} n_d(E)\, dE}, \quad (2)$$

where $n_d(E)$ is the *d*-band density of states at energy *E*.

3. RESULTS AND DISCUSSION

3.1 Thermodynamics and Stability of Pt/WC Interfaces

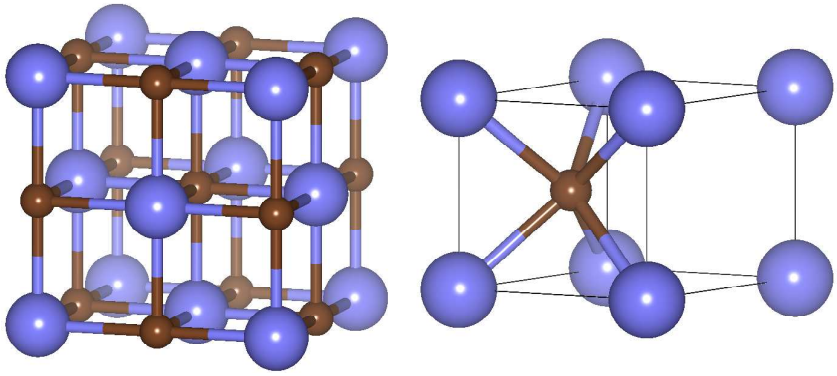

Figure 1. Unit cells of (a) β-WC and (b) α-WC (W – large blue spheres; C – small, brown spheres)

As noted previously, we focus here on two forms of WC: the low-temperature hexagonal-close-packed phase (α-WC) and the high-temperature, face-centered-cubic phase (β-WC) (Figure 1). The calculated lattice parameters for the two phases are reported in Table 1 and seen to be in excellent agreement with experimental data.[49,50] The calculated heats of formation of the two phases (at 0K) also confirm the stability of α-WC relative to β-WC and are in agreement with previous reports.[39,51,52]

Of the various possible low-Miller index surfaces of α-WC and β-WC for deposition of Pt overlayers, we restrict attention here to W-terminated α-WC (001), β-WC (001), and β-WC (111) surfaces as these are the most relevant surfaces and/or Pt/WC interfaces observed in experiments.[7, 20-25] Our independent DFT studies of various low-Miller surfaces (Figure S1) confirm that the aforementioned surfaces are indeed energetically preferred over a wide range of chemical potentials. Furthermore, we have also confirmed that interfaces between Pt overlayers and C-terminated surfaces are thermodynamically unfavorable, which further justifies our focus on W-terminated slab models for the WC supports.[14,39] From here on, for brevity, we simply

refer to the WC slabs by their surface orientation [e.g., α-WC (001)] with the implicit understanding that the surface/interface of interest is W-terminated unless otherwise specified.

Table 1. Comparison of calculated and experimental (in parentheses) lattice parameters of bulk WC and TiC, and their calculated heats of formation (ΔH_f) at 0K; μ_{WC}, μ_{TiC}, μ_W, μ_{Ti}, and μ_C are the calculated chemical potentials (at 0K) of WC, TiC, W, Ti, and C, respectively

	***a* (Å)**	***c* (Å)**	$\Delta H_f = \mu_{WC/TiC} - \mu_{W/Ti} - \mu_C$ **(eV)**
α-WC	2.92 (2.91) [49]	2.85 (2.84) [49]	-0.28
β-WC	4.38 (4.38) [49, 50]	-	+0.64
β-TiC	4.32 (4.32) [53]	-	-1.54

Prior to studying the energetics of hydrogen adsorption on WC-supported Pt, we seek to understand first the relative stability of different Pt/WC interfaces. The stability of the Pt/WC interfaces is characterized by their formation energy on an interfacial area basis, E_f, defined as

$$E_f = \frac{E_{Pt/WC} - N_{Pt}\mu_{Pt} - N_W\mu_W - N_C\mu_C}{A}, \quad (3)$$

where $E_{Pt/WC}$ is the total energy of the composite Pt/WC slab; N_{Pt}, N_W, and N_C represent the number of Pt, W, and C atoms, respectively, with corresponding chemical potentials μ_{Pt}, μ_W, and μ_C; and A is the total surface area of the symmetric slab. The reference chemical potentials are obtained from 0K DFT calculations using fcc Pt, bcc W, α/β-WC and graphene as the reference phases. The formation energies are then calculated as a function of the chemical potential of carbon, μ_C, under the constraints [54,55]

$$\mu_W + \mu_C = \mu_{\alpha/\beta-WC}, \quad (4)$$

and

$$\mu_{C,graphene} + \Delta H_{f,\alpha/\beta-WC} < \mu_C < \mu_{C,graphene}, \quad (5)$$

where $\Delta H_{f,\alpha/\beta\text{-}WC}$ is the heat of formation for α/β-WC, reported in Table 1. A key issue that must be accounted for when considering the stability of the Pt/WC interface is the influence of lattice mismatch between the Pt overlayers and the WC support. In particular, the support can exert a so-called "strain effect" [13,14,22] on the catalytic properties of the Pt overlayer and we would like to understand this effect independent of artificial lattice matching between Pt and WC in the computational model. To this end, we consider not only lattice-matched Pt overlayers on WC but also explore larger coincident-site lattices between Pt overlayers and the WC supports. Yates *et al*.[14] examined these mismatch strain effects by considering extended surface cells that allow for better lattice matching between Pt overlayers and WC supports; we go beyond their work by also including rotations of the Pt overlayer in an effort to minimize mismatch strains. It is not possible to examine a large number of rotated and lattice-matched surface cells with DFT calculations and so we focus on a few candidates that allow us to critically examine the effects of mismatch strain while, at the same time, keeping the calculations tractable. The various supercells studied are listed in Table S1. In finding commensurate surface cells only the Pt layer is rotated and expanded/contracted to match the underlying WC slab.[56] As the expansion/contraction can be different along the two supercell vectors, we quantify the net strain as an areal mismatch defined via a misfit factor (η)[57] as

$$\eta = \frac{A_{WC} - A_{Pt}}{A_{WC} + A_{Pt}} \quad (6)$$

where A_{WC} is the surface area of WC slab (support) and A_{Pt} is the surface area of the commensurate Pt layer when it is unstrained.

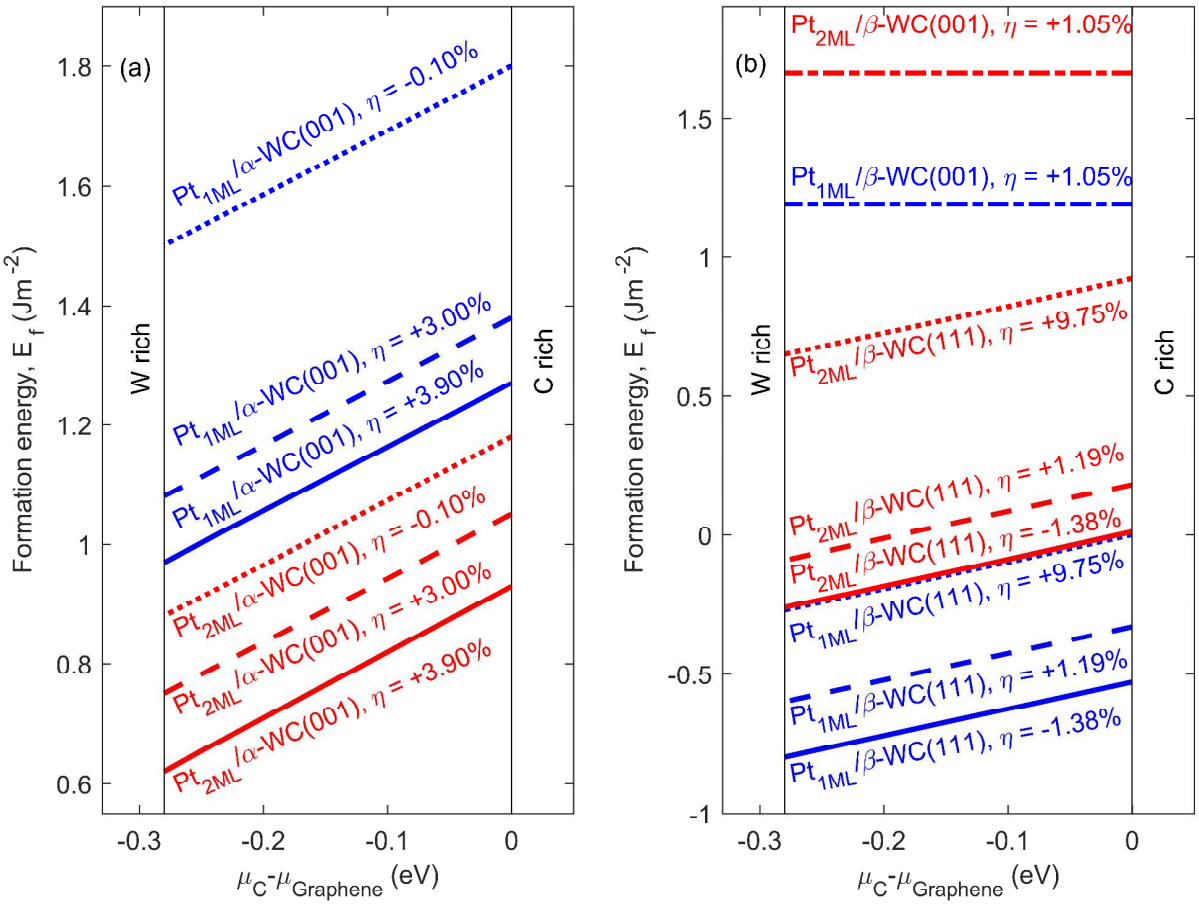

Figure 2. Formation energies (E_f) of 1-2 Pt MLs over (a) α-WC (001) and (b) β-WC (111) support in various surface unit-cells (reported in Table S1) with different misfit factors (η), as a function of the chemical potential of carbon (relative to graphene).

We consider first a monolayer of Pt on the α-WC (001) surface – Pt_{ML}/α-WC (001) (Slab 1, Table S1). The atoms of the α-WC (001) surface are arranged in a triangular lattice (close packed) and a simple arrangement of Pt atoms filling the hollow surface sites, i.e., a p-(1x1) R0° unit cell, leads to an epitaxially matched Pt (111) ML at +3.9% equibiaxial strain (η=+3.9%).[22] This large mismatch strain can be reduced to +3.00% in a larger supercell (Slab 2, Table S1) and to an even smaller value of -0.10% for the p-(4x4) R15° supercell (Slab 3, Table S1).[56] As seen from Figure 2 (a), the formation energy of the p-(4x4) R0° supercell is lower than the two rotated Pt MLs in spite of the latter MLs possessing smaller overall mismatch strains. The reason for

this, possibly counterintuitive, result is that the ligand effect arising from the optimal coordination of Pt atoms at surface hollow sites far outweighs the strain effect from epitaxial mismatch.[22] Furthermore, we also observe from the relaxed structures (Figure S2) that the rotated MLs display significant in-plane structural distortions with regions of both compressive and tensile strain indicative of less-than-optimal bonding with the support. Upon addition of a second epitaxially-matched Pt monolayer we find that the formation energy of the composite Pt/WC (001) system decreases by ~0.4 J/m^2. In conjunction with the fact that the formation energy of the ML is positive (thermodynamically unfavorable) over a wide range of chemical potentials, this result explains why Pt nucleates as clusters rather than contiguous layers on α-WC (001) surfaces in experiments.[28,29,31] The thermodynamics of island nucleation on α-WC (001) is beyond the scope of this work and will be reported elsewhere. For the β-WC supports, we considered two possible surface orientations—the stoichiometric (001) surface, which consists of both W and C atoms arranged on a centered square lattice and the close-packed, W-terminated (111) surface. For the case of Pt_{ML}/β-WC (001), we constructed a commensurate surface supercell with a misfit factor, η=+1.05% (Slab 4, Table S1); the formation energy [Figure 2 (b)] in this case (~1.2 J/m^2) is independent of μ_C and comparable to that for p-(4x4) R0° Pt_{ML}/α-WC (001). Adding another monolayer of Pt to this Pt_{ML}/β-WC (001) supercell increases the formation energy of Pt_{2ML}/β-WC (001) by ~0.5 J/m^2; this is unlike the Pt/α-WC (001) case wherein the addition of the second Pt ML is thermodynamically favored. In contrast to the Pt/β-WC (001) case, all Pt_{ML}/β-WC (111) slabs (Slabs 5, 6 & 7; Table S1) display negative formation energies over the same range of μ_C values. Interestingly, the two rotated Pt ML cases (Slab 6, η=+1.19%; Slab 7, η=-1.38%; Table S1) now display *lower* formation energies [Figure 2(b)] than the epitaxially-matched Pt ML that has a large misfit of η=+9.75%. Indeed, Hendon *et*

al.[13] have used *ab initio* molecular dynamics (AIMD) simulations and shown that an epitaxially-matched Pt ML on β-$Ti_{0.1}W_{0.9}C$ (111) spontaneously develops defects and fractures into smaller islands. We also note from Figure 2(b) that the Pt ML with η=-1.38% misfit (Slab 7; Table S1) is thermodynamically favored, somewhat counterintuitively, over the Pt ML with η=+1.19% (Slab 6; Table S1), which once again points to a delicate balance between ligand and strain effects at the Pt/WC interface. Furthermore, upon deposition of a second layer of Pt on these two MLs (i.e., the η=-1.38% and η=+1.19% cases) we find that the formation energy actually increases (by ~0.5 J/m^2). Thus, unlike our earlier observation for Pt/α-WC (001), we now find that the β-WC (111) surface preferentially stabilizes a single layer of Pt over a bilayer. For completeness, we performed AIMD simulations of the most thermodynamically favorable Pt_{ML}/β-WC (111) and Pt_{ML}/β-WC (001) structures (Figures S3 and S4) and did not observe any significant structural changes (fracture, clustering, debonding, etc.) up to temperatures of 1000 K over 0.5 ps of simulation time.

Based on the above thermodynamic analyses, we may now conclude that the β-WC phase is well suited for stabilizing 1-2 Pt MLs, which is consistent with experimental reports on β-TiWC@Pt core-shell nanoparticles.[15,34] The α-WC phase, on the other hand, favors clustering of Pt during the initial stages of growth. Furthermore, we may also conclude that the Pt/β-WC (111) interface is energetically favored over the Pt/β-WC (001) interface, which is consistent with powder x-ray diffraction (PXRD) studies of β-$Ti_{0.1}W_{0.9}C$@Pt core-shell nanoparticles[15,34] that indicate the dominance of (111) facets over (001) facets.

3.2 Alloying of β-WC with Ti

In recent experiments, Hunt *et al.*[15,34,58] showed that thermodynamic stability of WC nanoparticles can be enhanced by alloying with elements such as Ti or Ta, which are known to form some of the most stable carbides (TiC and TaC).[59] However, the influence of such bimetallic carbide supports on the stability and electronic structure of Pt MLs is still not fully understood. First, to confirm the stabilizing effect of Ti, we consider the thermodynamics of alloying of β-WC with Ti. As TiC and β-WC both display rock-salt crystal structures with very similar lattice constants ($a_{\beta\text{-WC}}$ =4.38 Å [49,50] and a_{TiC}=4.32 Å [53]), we constructed bulk alloy supercells by simple substitutional exchange of W with Ti atoms. The heat of formation of the alloy (per metal-carbide pair), ΔH_f^{alloy}, was computed as

$$\Delta H_f^{alloy} = \frac{\mu_{Ti_xW_{1-x}C} - N_{Ti}\mu_{Ti} - N_W\mu_W - N_C\mu_C}{N_{MC}}, \quad (7)$$

where $\mu_{Ti_xW_{1-x}C}$ is the DFT energy (0K) of the alloy supercell, x is the fraction of Ti atoms, and N_{MC} is the number of metal-carbide (WC and TiC) pairs. Figure 3 displays the heat of formation of the $Ti_xW_{1-x}C$ alloy as a function of Ti content from which we observe that alloying with Ti indeed has a stabilizing effect on the β-WC phase. Specifically, in our DFT calculations, the formation of the rock-salt $Ti_xW_{1-x}C$ alloy structure transitions from endothermic to exothermic at ~20% Ti-doping. As an additional check on these results, we also report in Fig. S9 the alloy heats of formation using the PBE+U approach[60], which can account partially for strongly-correlated *d*-electrons of Ti, and a more accurate meta-GGA (SCAN[61]) exchange-correlation functional; all approaches confirm the trends in ΔH_f^{alloy} with increasing Ti content and including the stabilization of the β-WC phase at ~20% Ti doping. Free-energy calculations for these

systems that explore the thermodynamics at elevated temperatures, typical of synthetic conditions, will be reported elsewhere.

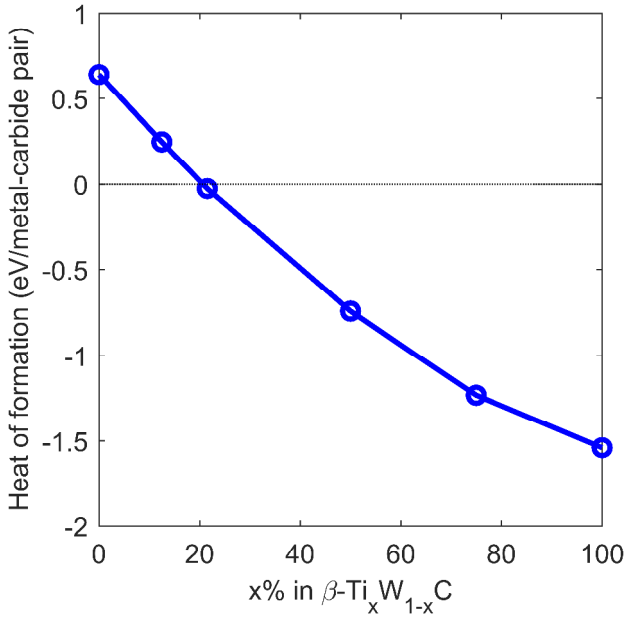

Figure 3. Heat of formation of β-$Ti_xW_{1-x}C$ alloy, ΔH_f^{alloy} (Eq. 7), as a function of Ti content (x%)

While the TiWC alloy bulk is reasonably represented by random substitution of W with Ti, we need to account for the possibility of Ti segregation/desegregation at surfaces or interfaces in our slab models. To this end, we calculated the heat of formation of β-WC (111) and Pt/β-WC (111) slabs as a function of position of the Ti dopant atom relative to the slab surface (Supporting Information). As seen from Figure S5(a), for β-WC (111) slabs, Ti substitution is energetically preferred in the subsurface layers and, in particular, within the first subsurface W-layer. In the case of the Pt/β-WC (111) slab [Figure S5(b)], substitution of W sites within the surface layer is only slightly energetically disfavored. Thus, we proceed for now to construct Pt/β-$Ti_xW_{1-x}C$ slabs by random substitution of a fraction x of W atoms with Ti atoms. Prior

studies[13] have ignored these issues of surface segregation/desegregation of Ti and, as we show in Table S2, the implications for hydrogen binding can, in some instances, be non-negligible.

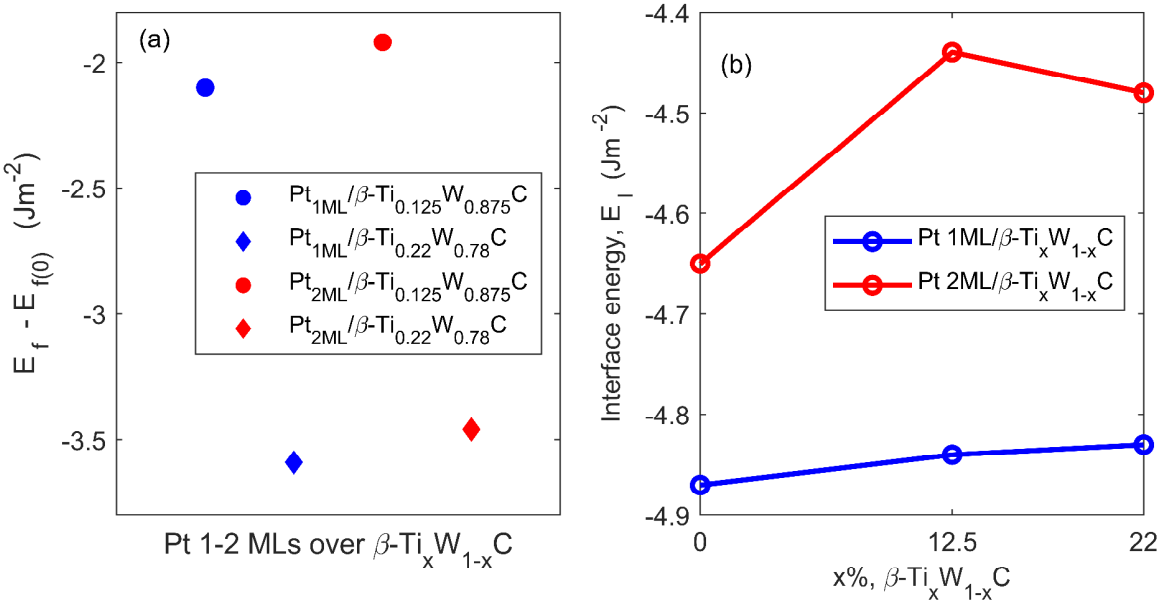

Figure 4. (a) Formation energy (per unit interface area), E_f, of 1-2 MLs of Pt over β-$Ti_xW_{1-x}C$ (111) supports relative to their corresponding values on undoped β-WC (111). (b) Interface energy, E_I, of 1-2 MLs of Pt over β-$Ti_xW_{1-x}C$ as a function of Ti concentration (x%).

In Figure 4(a), we display the difference between the formation energies (E_f) of 1-2 Pt MLs on β-$Ti_xW_{1-x}C$ (111) supports and their corresponding formation energies on undoped β-WC (111) [$E_{f(0)}$]; the individual formation energies are calculated as

$$E_f = \frac{E_{Pt/TiWC} - N_{Pt}\mu_{Pt} - N_W\mu_W - N_{Ti}\mu_{Ti} - N_C\mu_C}{A}, \quad (8)$$

where $E_{Pt/TiWC}$ is the total energy of the composite Pt/TiWC slab; N_{Pt}, N_W, N_{Ti} and N_C represent the number of Pt, W, Ti and C atoms, respectively, with corresponding chemical potentials μ_{Pt}, μ_W, μ_{Ti}, and μ_C; and A is the total surface area of the symmetric slab. As the thermodynamics of the ternary Ti-W-C system is beyond the scope of this work, for simplicity, we use the 0K DFT

energies of bulk fcc Pt, bcc W, hcp Ti and graphene as the relevant chemical potentials in Eq. 8. From Figure 4(a), we see that for each support, the formation of 1 ML Pt is thermodynamically preferred over 2 MLs and, furthermore, the alloying of β-WC with Ti has a stabilizing effect on the energetics of the Pt/β-$Ti_xW_{1-x}C$ (111) system. To understand further whether this stabilization upon addition of Ti arises from the increased stability of the core (Figure 3) or the formation of a more stable core-shell interface, we calculated the interface energy, E_I, of 1-2 Pt MLs over β-$Ti_xW_{1-x}C$ supports [Figure 4(b)]. The interface energy is defined as

$$E_I = \frac{E_{Pt/TiWC} - E_{TiWC} - E_{Pt}}{A}, \quad (9)$$

where $E_{Pt/TiWC}$ is the energy of the Pt/TiWC slab, E_{TiWC} is the energy of the TiWC slab, E_{Pt} is the energy of the isolated Pt (111) monolayer or bilayer in vacuum, and A is the total surface area of the Pt/TiWC slab. From Figure 4(b), we note that all 1-2 ML Pt/β-$Ti_xW_{1-x}C$ interfaces are thermodynamically favorable, but the interface energies increase slightly with added Ti. Thus, the principal effect of Ti is to stabilize the β-$Ti_xW_{1-x}C$ support (core) rather than the Pt/β-$Ti_xW_{1-x}C$ interface.

3.3 Hydrogen Binding Energies on Pt/WC and Pt/$Ti_xW_{1-x}C$

Having examined the thermodynamics of various Pt/WC and Pt/$Ti_xW_{1-x}C$ systems, we now turn to the question of hydrogen binding energies (HBEs), a key descriptor of the catalytic activity of surfaces for the hydrogen evolution reaction (HER).[23,62–64] As the supported Pt layers undergo structural distortions leading to variations in the surface strain, we first sampled several binding sites within regions of compressive and tensile strains (Table S3). As expected [65,66] adsorption sites with compressive strains displayed lower—and sometimes thermodynamically unfavorable—HBEs than those with tensile strains.

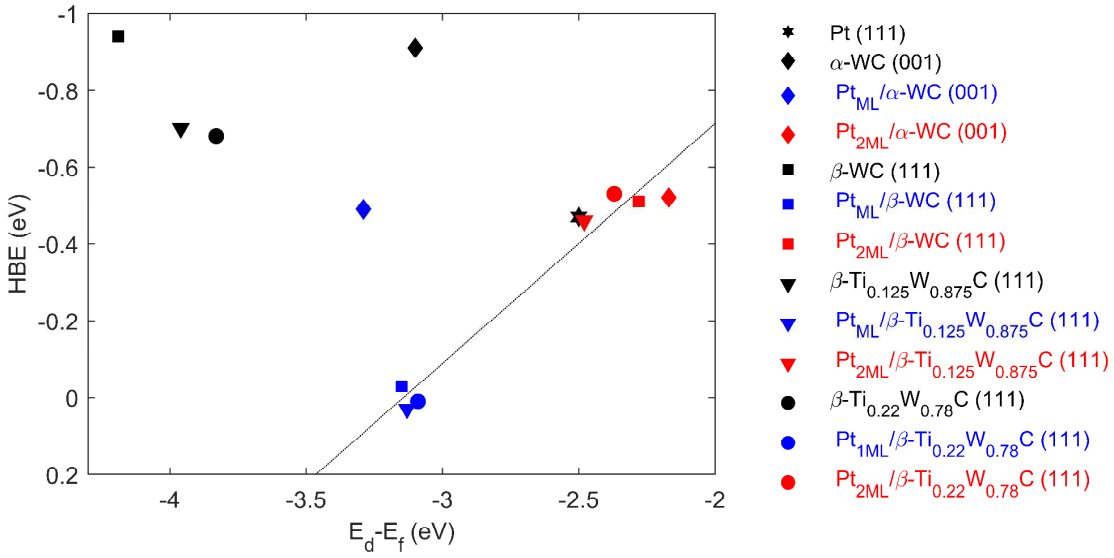

Figure 5. Hydrogen binding energy (HBE) versus the *d*-band center relative to the Fermi-level (E_d-E_f) of the Pt surface; the solid line is a guide to the eye that shows a subset of the data that follow the *d*-band model, namely, most of the α-/β-WC@Pt and α-/β-$Ti_xW_{1-x}C$@Pt systems

For transition-metal surfaces, it is well known that the binding energy of adsorbates is correlated with the *d*-band center energy of the surface.[67] Thus, we sought to investigate whether the *d*-band center energy is also a good descriptor for HBE in our systems. Figure 5 displays the (most stable) HBEs for the most stable surfaces identified previously as a function of the *d*-band center of the surface. We observe readily that one set of data, namely, that for 1-2 Pt MLs over α-WC, β-WC and β-$Ti_xW_{1-x}C$ supports—with the notable exception of Pt_{ML}/α-WC (001)—all follow the *d*-band model. A second set of data consists of large outliers, namely, the bare transition-metal carbide surfaces α-WC (001), β-WC (111), and β-$Ti_xW_{1-x}C$ (111) that

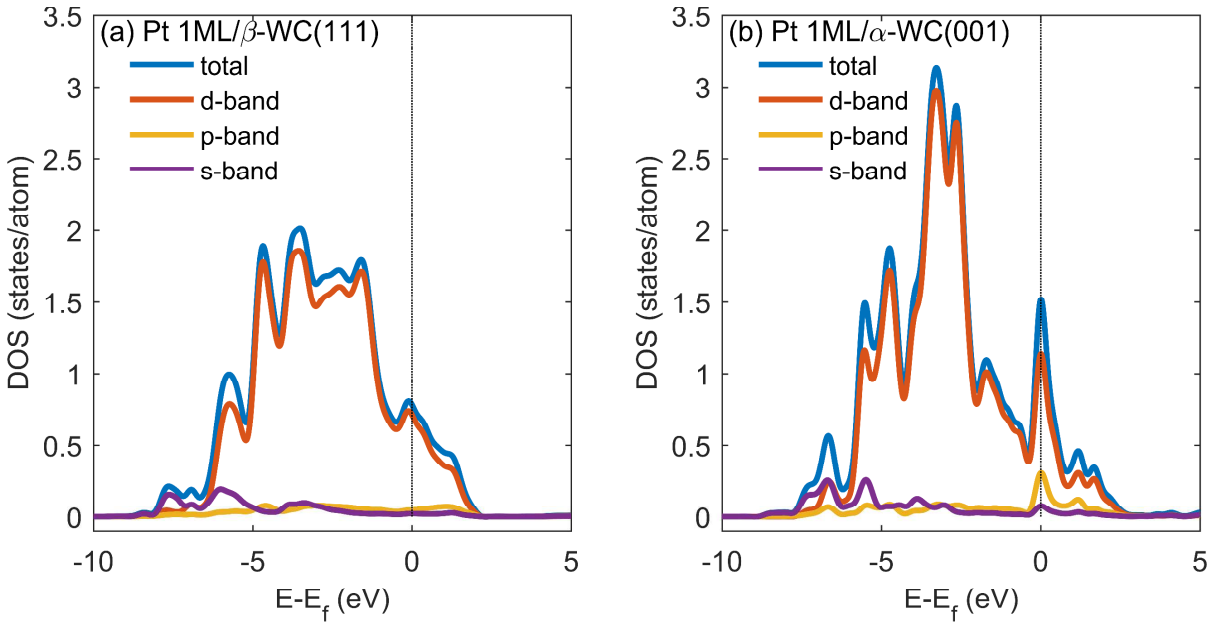

Figure 6. Total and angular-momentum-projected density of states of (a) Pt_{ML}/β-WC (111) and (b) Pt_{ML}/α-WC (001) slabs

are known from previous studies[12,14] to violate the *d*-band model. Kitchin *et al.*[12] have attributed the failure of the *d*-band model for H adsorption on TMC surfaces to the inaccurate description of the *d*-band of TMC surfaces by DFT due to the overcounting of low-energy states from nearby C atoms that lower the *d*-band center. To understand the outlying case of Pt_{ML}/α-WC (001), which has similar *d*-band center energy as Pt_{ML}/β-WC (111) but an unexpectedly higher HBE (by ~0.5 eV), we probed the electronic structure of these two surfaces in detail. Figure 6 displays the total as well as angular-momentum projected density of states for these two slab models from which we observe that the Pt_{ML}/α-WC (001) system has a large resonance in the density of *d*-states at the Fermi level. Further analysis (Figure S6) reveals that this resonance has a large contribution from the Pt ML, which explains the increased affinity of H for this surface. With respect to the role of Ti addition to the supports, we find negligible differences in the electronic structure of supported Pt MLs (even up to 22% doping) as seen from the similar *d*-band center

positions and bandwidths of Pt_{MLs}/β-$Ti_xW_{1-x}C$ (111), x = 0, 0.125, 0.22 (Figure S7). However, the HBEs of bare β-$Ti_xW_{1-x}C$ (111) surfaces do indeed decrease with increasing Ti doping, which may be expected from the hole-doping effect of Ti.

The connection between HBEs and the activity of the various WC and Pt/WC surfaces can be made via Sabatier's principle,[69] which is visually rendered by the so-called "volcano plot". For HER, in particular, Esposito *et al.*[18] have shown that the optimal HBE is ~0.37 eV, which is ~0.1 eV more positive than the corresponding value for Pt (111). Figure 7 displays our calculated HBEs superposed over the volcano plot of Esposito *et al.*[18] who reported the HER activities of various transition metals, transition-metal carbides, and transition-metal-carbide-supported transition metals. While we have not calculated exchange currents independently in this work, superimposing our data, based on their abscissas (HBEs), over the well-established volcano curve allows us to make some preliminary estimates for our systems.[70] The most significant observation from Figure 7 is that the anticipated exchange current densities for Pt_{2ML}/β-$Ti_{0.125}W_{0.875}C$ (111) is comparable, if not slightly greater, than that for Pt (111), which is among the best HER catalysts. This is consistent with recent experimental findings of Hunt *et al.*[15,34] who found the HER activity of Pt/β-$Ti_{0.1}W_{0.9}C$ core-shell nanoparticles to be superior to that of Pt (111). On the other hand, we observe that Pt_{ML}/α-WC (001) and Pt_{2ML}/α-WC (001), while towards the upper end of the volcano, are less active than Pt (111), which indicates that the metastable β-WC phase is more desirable as a support material than the ground-state α-WC phase. We also observe that 12.5% Ti-doping of β-WC yields a more active catalyst than the 22% Ti-doped case as seen from the lower predicted activity when employing the latter as a support.

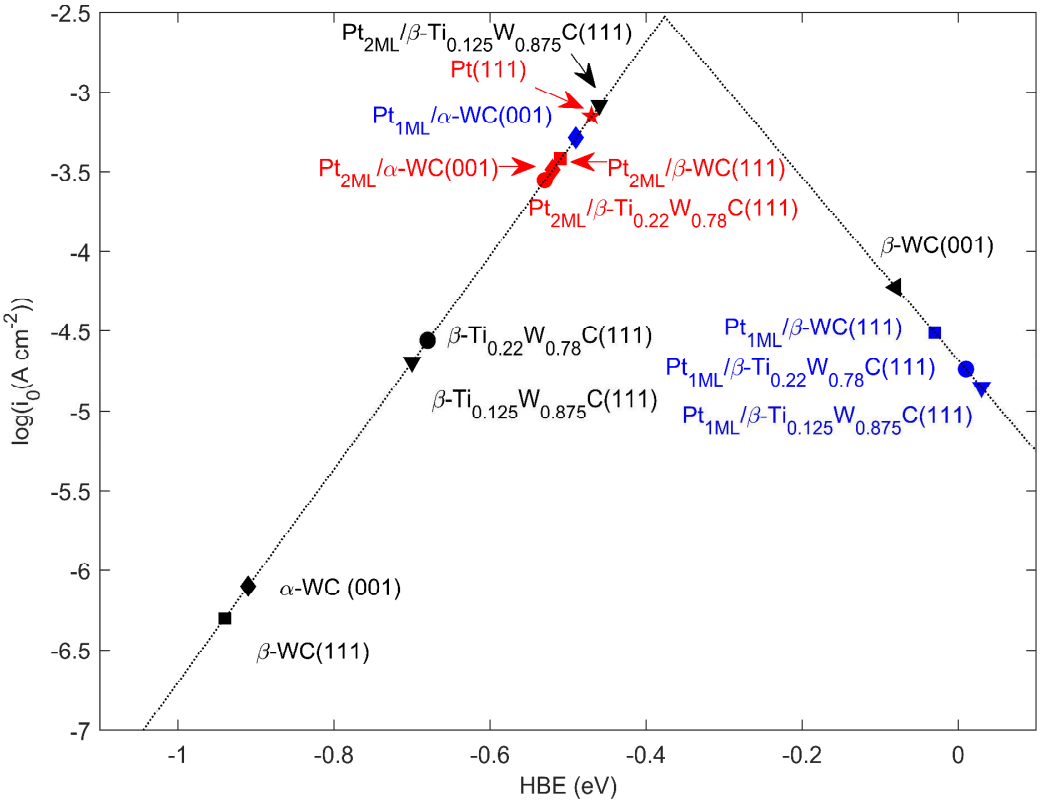

Figure 7. Volcano plot for HER showing the exchange current densities ($\log(i_o)$) plotted as a function of hydrogen binding energy. The exchange current densities are estimated by superimposing our data for various surfaces, based on their calculated HBEs, over the volcano plot reported in Ref. 18

The analysis of catalytic activity thus far has been based on HBEs at the most stable binding sites. There are, of course, variations in HBEs over a given Pt overlayer due to a combination of ligand and strain effects arising from the interaction of the overlayer with the support. Complete surface scans of HBEs for all systems studied here are prohibitively expensive. Nevertheless, by focusing on the most promising HER catalysts identified above, namely, $Pt_{2ML}/\beta\text{-}Ti_xW_{1-x}C$ (x=0%, 12.5%, 22%) it is possible to estimate the sensitivity of our predictions to such variations in HBEs. We ordered the H-binding sites on the Pt overlayers (top, bridge, hollow) by their site-

projected *d*-band centers[71] and sampled several sites to span the range of *d*-band energies (Table S4). We find that the spread of HBEs (Table S4; Figure S10) is at most ~0.2 eV for the three $Pt_{2ML}/\beta\text{-}Ti_xW_{1-x}C$ (x=0%, 12.5%, 22%) systems studied here. We also find (Figure S10) that, upon including a multitude of binding sites in the analysis, the correlation between the site-projected *d*-band center and the HBE is weaker than before (i.e., with most stable adsorption sites; Figure 5) although this has no impact on the volcano-plot analysis, which is based on HBEs alone. The key point of note here is that our volcano-plot analysis is a conservative one, being based on the largest HBEs, and the inclusion of weaker binding sites for the $Pt_{2ML}/\beta\text{-}Ti_xW_{1-x}C$ systems will, on average, push the expected values of exchange currents further towards the peak of the volcano. A more complete analysis must also take into account surface coverage effects, which is deferred to future work.

4. CONCLUSIONS

In summary, using first-principles DFT calculations we investigated the thermodynamic stability, electronic structure, and HER activity of 1-2 layers of Pt on α-WC and $\beta\text{-}Ti_xW_{1-x}C$ supports. The main finding from our thermodynamic studies is that 1-2 layers of Pt are more stable on $\beta\text{-}Ti_xW_{1-x}C$ (111) supports than on α-WC (001), which indicates that $\beta\text{-}Ti_xW_{1-x}C$@Pt core-shell nanoparticles will be more stable than α-WC@Pt core-shell nanoparticles. Moreover, the addition of Ti to β-WC improves the stability of the β-WC support and, correspondingly, the stability of the $\beta\text{-}Ti_xW_{1-x}C$@Pt core-shell nanoparticles, without significantly affecting the desired catalytic and electronic properties of the Pt shell. These results are in agreement with experimental reports of the stabilization of the high-temperature β-WC phase by Ti doping/alloying in $\beta\text{-}Ti_xW_{1-x}C$@Pt core-shell nanoparticles.[15,34] We estimated the HER activities

of Pt/WC surfaces from their HBEs and arrived at two key observations about 1-2 Pt layers on α- and β-WC supports. While Pt_{ML}/β-WC (111) and Pt_{ML}/α-WC (001) have comparable *d*-band center energies, the former is relatively inactive for HER whereas the latter, due to a larger resonance in *d*-states at the Fermi level, has an activity comparable to Pt (111). The addition of an extra monolayer of Pt improves the activity of all Pt_{2ML}/β-$Ti_xW_{1-x}C$ (111) systems studied here and these catalysts become significantly more active for HER approaching Pt (111). We examined the effect of Ti doping of the WC supports and found the addition of Ti improves the stability of the supports while mostly retaining the overall activity of the Pt overlayers. Specifically, Pt_{2ML}/β-$Ti_{0.125}W_{0.875}C$ is predicted to be as active as the Pt (111) surface with Pt_{2ML}/β-$Ti_{0.125}W_{0.875}C$ benefiting from the added stability of the core from the added Ti. Overall, we find that the phase of the WC support has a significant influence of the catalytic activity of the Pt overlayers and that the high-temperature β-WC phase (with or without Ti doping) will be a better support material for Pt monolayers than the room-temperature α-WC phase. Future experiments that compare systematically the morphological stability of Pt overlayers on the α and β phases of WC (doped and undoped), and correlate morphology with activity could offer significant insights towards optimizing these materials for electrocatalytic HER.

More broadly, this work opens up interesting avenues for further exploration of support effects on the activity of catalytic overlayers, in particular, via high-throughput, combinatorial, first-principles studies that explore the effects of binary TMC supports on supported transition-metal catalysts. In conjunction with descriptor-based analyses (e.g., binding energies of hydrogen and oxygen for HER and ORR, respectively), such studies could help guide the rational design of core-shell catalysts and will be explored in future work.

ACKNOWLEDGEMENTS

We gratefully acknowledge research funding from the U.S. Department of Energy under Award Number DE-SC0010610. This research used resources of the National Energy Research Scientific Computing Center, a DOE Office of Science User Facility supported by the Office of Science of the U.S. Department of Energy under Contract No. DE-AC02-05CH11231.

REFERENCES

1 T. G. Kelly and J. G. Chen, *Chem. Soc. Rev.*, 2012, **41**, 8021–8034.

2 M. M. Sullivan, C.-J. Chen and A. Bhan, *Catal. Sci. Technol.*, 2016, **6**, 602–616.

3 K. Xiong, W. Yu and J. G. Chen, *Appl. Surf. Sci.*, 2014, **323**, 88–95.

4 D. J. Ham and J. S. Lee, *Energies*, 2009, **2**, 873–899.

5 Y. Liu, T. G. Kelly, J. G. Chen and W. E. Mustain, *ACS Catal.*, 2013, **3**, 1184–1194.

6 Y. Zhong, X. Xia, F. Shi, J. Zhan, J. Tu and H. J. Fan, *Adv. Sci.*

7 A.-M. Alexander and J. S. J. Hargreaves, *Chem. Soc. Rev.*, 2010, **39**, 4388–4401.

8 G. Ertl, H. Knözinger, F. Schüth and J. Weitkamp, 2008, **Vol. 1**, 342–356.

9 R. B. Levy and M. Boudart, *Science (80-.).*, 1973, **181**, 547 LP-549.

10 F. Calle-Vallejo, A. Krabbe and J. M. García-Lastra, *Chem. Sci.*, 2017, **8**, 124–130.

11 H. Shin, Y. Ha and H. Kim, *J. Phys. Chem. Lett.*, 2016, **7**, 4124–4129.

12 J. R. Kitchin, J. K. Nørskov, M. A. Barteau and J. G. Chen, *Catal. Today*, 2005, **105**, 66–73.

13 C. H. Hendon, S. T. Hunt, M. Milina, K. T. Butler, A. Walsh and Y. Román-Leshkov, *J. Phys. Chem. Lett.*, 2016, **7**, 4475–4482.

14 J. L. R. Yates, G. H. Spikes and G. Jones, *Phys. Chem. Chem. Phys.*, 2015, **17**, 4250–

4258.

15 S. T. Hunt, M. Milina, A. C. Alba-Rubio, C. H. Hendon, J. A. Dumesic and Y. Román-Leshkov, *Science (80-.).*, 2016, **352**, 974–978.

16 D. V Esposito, S. T. Hunt, A. L. Stottlemyer, K. D. Dobson, B. E. McCandless, R. W. Birkmire and J. G. Chen, *Angew. Chemie Int. Ed.*, 2010, **49**, 9859–9862.

17 B. M. Tackett, W. Sheng and J. G. Chen, *Joule*, 2017, 253–263.

18 D. V. Esposito, S. T. Hunt, Y. C. Kimmel and J. G. Chen, *J. Am. Chem. Soc.*, 2012, **134**, 3025–3033.

19 F. de Bruijn, *Green Chem.*, 2005, **7**, 132.

20 M. B. Chris, H. Michael, L. Zhang, L. Wang, C. M. B. Holt, T. Navessin and K. Malek, *Discover*, 2010, 16463–16474.

21 K. H. Kangasniemi, D. A. Condit and T. D. Jarvi, *J. Electrochem. Soc.*, 2004, **151**, E125.

22 H. Zhuang, A. J. Tkalych and E. A. Carter, *J. Electrochem. Soc.*, 2016, **163**, F629–F636.

23 D. V Esposito and J. G. Chen, *Energy Environ. Sci.*, 2011, **4**, 3900–3912.

24 C. Ma, T. Liu and L. Chen, *Appl. Surf. Sci.*, 2010, **256**, 7400–7405.

25 H. Chhina, S. Campbell and O. Kesler, *J. Electrochem. Soc.*, 2007, **154**, B533.

26 R. R. Adzic, J. Zhang, K. Sasaki, M. B. Vukmirovic, M. Shao, J. X. Wang, A. U. Nilekar, M. Mavrikakis, J. A. Valerio and F. Uribe, *Top. Catal.*, 2007, **46**, 249–262.

27 M. B. Vukmirovic, J. Zhang, K. Sasaki, A. U. Nilekar, F. Uribe, M. Mavrikakis and R. R. Adzic, *Electrochim. Acta*, 2007, **52**, 2257–2263.

28 I. J. Hsu, J. G. Chen, X. Jiang and B. G. Willis, *J. Vac. Sci. Technol. A Vacuum, Surfaces, Film.*, 2015, **33**, 01A129.

29 I. J. Hsu, Y. C. Kimmel, X. Jiang, B. G. Willis and J. G. Chen, *Chem. Commun.*, 2012, **48**,

1063.

30 I. J. Hsu, Y. C. Kimmel, Y. Dai, S. Chen and J. G. Chen, *J. Power Sources*, 2012, **199**, 46–52.

31 I. J. Hsu, D. A. Hansgen, B. E. Mccandless, B. G. Willis and J. G. Chen, *J. Phys. Chem. C*, 2011, **115**, 3709–3715.

32 A. Garg, M. Milina, M. Ball, D. Zanchet, S. T. Hunt, J. A. Dumesic and Y. Román-Leshkov, *Angew. Chemie - Int. Ed.*, 2017, **56**, 8828–8833.

33 S. T. Hunt, T. Nimmanwudipong and Y. Román-Leshkov, *Angew. Chemie - Int. Ed.*, 2014, **53**, 5131–5136.

34 S. T. Hunt, M. Milina, Z. Wang and Y. Roman-Leshkov, *Energy Environ. Sci.*, 2016, 3290–3301.

35 D. D. Vasić, I. A. Pašti and S. V Mentus, *Int. J. Hydrogen Energy*, 2013, **38**, 5009–5018.

36 D. D. Vasić Anićijević, V. M. Nikolić, M. P. Marčeta-Kaninski and I. A. Pašti, *Int. J. Hydrogen Energy*, 2013, **38**, 16071–16079.

37 R. V. Sara, *J. Am. Ceram. Soc.*, 1965, **48**, 251–257.

38 D. V Suetin, I. R. Shein and A. L. Ivanovskii, *Russ. Chem. Rev.*, 2010, **79**, 611–634.

39 Y. Li, Y. Gao, B. Xiao, T. Min, Z. Fan, S. Ma and D. Yi, *Comput. Mater. Sci.*, 2011, **50**, 939–948.

40 G. Kresse and J. Furthmüller, *Phys. Rev. B*, 1996, **54**, 11169–11186.

41 G. Kresse and J. Furthmüller, *Comput. Mater. Sci.*, 1996, **6**, 15–50.

42 P. E. Blöchl, *Phys. Rev. B*, 1994, **50**, 17953–17979.

43 G. Kresse and D. Joubert, *Phys. Rev. B*, 1999, **59**, 1758–1775.

44 J. P. Perdew, K. Burke and M. Ernzerhof, *Phys. Rev. Lett.*, 1996, **77**, 3865–3868.

45 M. Methfessel and A. T. Paxton, *Phys. Rev. B*, 1989, **40**, 3616–3621.

46 G. Makov, *Phys. Rev. B*, 1995, **51**, 4014.

47 J. Neugebauer, *Phys. Rev. B*, 1992, **46**, 16067.

48 T. Bligaard and J. K. Nørskov, *Electrochim. Acta*, 2007, **52**, 5512–5516.

49 A. S. Kurlov and A. I. Gusev, *Russ. Chem. Rev.*, 2006, **75**, 617–636.

50 A. Vojvodic and C. Ruberto, *J. Phys. Condens. Matter*, 2010, **22**, 375501.

51 D. V. Suetin, I. R. Shein and A. L. Ivanovskii, *Phys. B Condens. Matter*, 2009, **404**, 1887–1891.

52 Y. Li, Y. Gao, B. Xiao, T. Min, Z. Fan, S. Ma and L. Xu, *J. Alloys Compd.*, 2010, **502**, 28–37.

53 M. H. K. Anderko and M. Hansen, *New York*.

54 J. E. Northrup and S. Froyen, *Phys. Rev. Lett.*, 1993, 71, 2276–2279.

55 J. E. Northrup and J. Neugebauer, *Phys. Rev. B*, 1995, 52, 17001–17004.

56 P. Lazić, *Comput. Phys. Commun.*, 2015, **197**, 324–334.

57 Z. Wang, X. Chen, Y. Cheng and C. Niu, *J. Phys. Chem. C*, 2015, **119**, 25684–25695.

58 S. T. Hunt, T. M. Kokumai, D. Zanchet and Y. Román-Leshkov, *J. Phys. Chem. C*, 2015, **119**, 13691–13699.

59 Y. C. Kimmel, X. Xu, W. Yu, X. Yang and J. G. Chen, *ACS Catal.*, 2014, **4**, 1558–1562.

60 S. L. Dudarev, G. A. Botton, S. Y. Savrasov, C. J. Humphreys and A. P. Sutton, *Phys. Rev. B*, 1998, **57**, 1505.

61 J. Sun, R. Haunschild, B. Xiao, I. W. Bulik, G. E. Scuseria and J. P. Perdew, *J. Chem. Phys.*, 2013, **138**, 44113.

62 R. Parsons, *Trans. Faraday Soc.*, 1958, **54**, 1053–1063.

63 R. Parsons, *Trans. Faraday Soc.*, 1960, **56**, 1340–1350.

64 J. K. Nørskov, T. Bligaard, a. Logadottir, J. R. Kitchin, J. G. Chen, S. Pandelov and U. Stimming, *J. Electrochem. Soc.*, 2005, **152**, J23.

65 M. Mavrikakis, B. Hammer and J. K. Nørskov, *Phys. Rev. Lett.*, 1998, **81**, 2819.

66 L. Grabow, Y. Xu and M. Mavrikakis, *Phys. Chem. Chem. Phys.*, 2006, **8**, 3369–3374.

67 B. Hammer and J. K. Nørskov, in *Advances in catalysis*, Elsevier, 2000, vol. 45, pp. 71–129.

68 J. R. Kitchin, J. K. Nørskov, M. A. Barteau and J. G. Chen, *Catal. Today*, 2005, **105**, 66–73.

69 P. Sabatier, *Catalysis in organic chemistry*, D. Van Nostrand Company, 1922.

70 Since our HBEs for Pt (111) and Pt_{ML}/α-WC (001) are in near exact agreement with the values reported by Esposito *et al*.,[18] we do not apply any additional corrections, i.e., energy shifts, to the HBEs.

71 For bridge and hollow sites, the *d*-band center energy is taken to be the average of the nearest-neighbor Pt atoms.

Table of Contents Figure

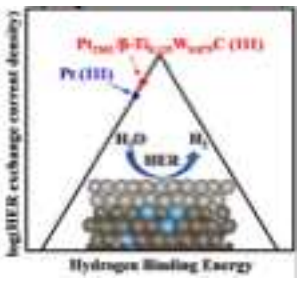

Titanium doping enhances the stability and activity of tungsten carbide core–platinum shell nanoparticles for hydrogen evolution